CrossMark

ORIGINAL ARTICLE

Effect of porosities on tensile properties of laser-welded Al-Li alloy: an experimental and modelling study

Enguang He[1] · Jun Liu[2] (iD) · Junyi Lee[2] · Kehuan Wang[2] ·
Denis J. Politis[2] · Li Chen[1] · Liliang Wang[2]

Abstract Aluminium–lithium (Al-Li) alloys are very attractive for aerospace applications due to their outstanding properties, such as high specific strength, high rigidity and good resistance to corrosion and fatigue, compared to conventional aluminium alloys. The butt joints of Al-Li 2A97-T3 alloy sheet produced by fibre laser welding with ER2319 filler wire were investigated in this paper. Uniaxial tensile tests have been performed to determine the nominal mechanical properties of the joints with and without porosities. In addition, a defect zone was defined in the welded specimens to investigate the effects of porosity on the joint tensile behaviour. The post-weld strength prediction (PWSP) model in a previous study has been extended by including the effects of the porosity in the welds to predict the overall response of the butt joints. The experimental and the modelling results show a good agreement, with the yield strength having a deviation lower than 5%. Both the yield strength and the ductility of the tensile specimens were observed to have decreased with the presence of porosities. The porosities aggravated the inhomogeneous deformation in the weld zone. Higher strain rate was found in the defect area than the remaining weld zone during plastic deformation, as the porosity in the specimen caused inhomogeneous deformation. It was found that this accelerated the failure of the specimen and lowered the global ductility significantly.

1 Introduction

Aluminium–lithium (Al-Li)-based alloys are excellent candidates for aircraft and aerospace structural materials. The addition of lithium not only reduces the material density but also significantly increases the elastic modulus, thereby increasing the specific strength and stiffness of the alloys [1, 2]. Among the various challenges facing the widespread use of Al-Li alloys in the aerospace sectors are the joining method selection and their impact on the mechanical properties of Al-Li weldment [3]. Arc welding of Al-Li based alloys has been comprehensively studied [4–6]. However, the results from these studies suggest that several issues, such as a large heat-affected zone (HAZ), large distortion, porosity, high residual stresses and poor mechanical properties are present in conventional fusion welding techniques [4–6]. On the other hand, laser beam welding (LBW) with its tight focusability and high power density of the laser beam can overcome those problems [7–9]. LBW is considered as an attractive welding method for production of aluminium alloys. It offers numerous advantages [10–12], e.g. high welding speed, narrow and deep weld, small HAZ, good mechanical properties, low structural distortion, etc. Moreover, the excellent propagation ability and accessibility make the LBW a powerful tool to produce three-dimensional structures with complicated features [13]. Thus, the structural integrity can be largely improved and the weldment weight is reduced through the optimisation of materials and structures. It was reported that LBW has been successfully

✉ Jun Liu
  jun.liu@imperial.ac.uk

✉ Liliang Wang
  liliang.wang@imperial.ac.uk

[1] Beijing Aeronautical Manufacturing Technology Research Institute, Beijing 100024, China

[2] Department of Mechanical Engineering, Imperial College London, London SW7 2AZ, UK

utilised as an alternative to riveting in manufacturing lower fuselage panels made of aluminium alloys [14]. By adopting the joining technology, improvements in product quality and properties and cost/weight saving for aircraft structural parts are also achieved through a modification of the structure design, a simplification of the manufacturing process and the elimination of additional elements such as rivets and sealants [15].

To expand its usage in aerospace structures, researchers have been attempting to develop LBW of Al-Li alloy thin sheets for medium strength applications. Although there is a huge potential for LBW to be used in Al-Li alloys [16, 17], the technique is not well understood currently. The welding parameters, keyhole dynamics, vapour and plasma characteristics, welding defects prevention and mechanical properties of the welded Al-Li alloy joints have been studied and reported in [18–20]. Porosity is a common defect encountered in the welds of aluminium alloys and is a critical problem in the LBW. The presence of porosity will reduce the effective area that is loaded in the weld and causes stress concentration. Moreover, pores may promote solidification cracking and is a key factor of fatigue crack nucleation [21].

Two types of porosity, i.e. metallurgical and keyhole pores, are usually found in the laser deep penetration weld of aluminium alloys [22, 23]. Metallurgical pores are generally spherical, have a smooth inner wall and are distributed homogeneously. Metallurgical pores are mainly related to hydrogen in the weld pool. These hydrogen pores can be found in the entire weld region, but most of them are located close to the fusion boundaries [24]. The formation mechanism of hydrogen porosity in LBW is similar to that of traditional fusion welding. It is generally accepted that the weld pool can absorb hydrogen resulting in supersaturation of the hydrogen. The excess hydrogen is then ejected from the liquid metal to form bubbles during cooling and solidification due to a decrease in hydrogen solubility, especially when there is a sharp reduction in the solidification temperature between the liquid and the solid phases. If the hydrogen bubbles are unable to escape the weld pool, they will remain as hydrogen pores once the metal solidifies.

On the other hand, keyhole pores are located predominantly in the centre of the weld and have been observed to have larger sizes and irregular shapes [25]. The formation of keyhole pores, including elongated and irregular root ones, is associated with the instability of the keyhole [26, 27]. The laser-induced plasma can influence the keyhole stability, and thus, keyhole porosity is a more significant problem in CO_2 laser welding than in YAG and fibre laser welding [28]. Due to the violent vaporisation of lithium during the welding of Al-Li alloys, the fraction of keyhole porosity is increased significantly [23], eventually leading to the process instability.

Research on the effects of porosities on the mechanical properties of welding joints of Al-Li alloy is very limited, as these effects are complicated and difficult to be captured. Numerical methods are considered to be the most effective

for understanding the deformation mechanisms during tensile loading. The rule of mixtures (ROM) model and finite element model utilising local constitutive behaviour have exhibited their capability in predicting the overall response of AA2024 friction stir welded specimens [29–31]. However, these studies do not include porosity or defects in their models.

In this study, butt joints of 2A97 alloys sheet with 1.5-mm thickness have been produced using fibre LBW with filler wire. The mechanical properties of tensile specimens with and without porosity were characterised, and the effect of porosity on the mechanical properties of joints was analysed. The post-weld strength prediction (PWSP) model from [19] was extended to investigate the effects of porosity on global mechanical response of the welded joints. This extended model, which incorporates plasticity theory in sheet metals and introduces defects in the weld, can predict the overall strengths accurately.

2 Experimental details

2.1 Material and welding method

Aluminium-lithium alloy 2A97 in the T3 temper was employed as the parent material in this study. Sheets with dimensions of 300 mm × 200 mm × 1.5 mm were welded along the rolling direction. The filler wire is ER2319 with a diameter of 1.2 mm. Approximately 0.1 mm of the surface layer of the sheets at both ends was removed via chemical milling to eliminate the oxidised layer and other surface contaminants. Table 1 summarises the chemical compositions of the base metal and the filler wire.

An IPG YLS-5000 fibre laser through a delivering diameter of 200 μm was used to create the butt joints. The focal diameter of the laser is 0.25 mm and is achieved by setting the focus lengths of the collimation lens to 200 mm and that of the focus lens of 250 mm. The laser power was 2 kW. All the welding processes in this work were conducted at a welding speed of 1.8 m/min and a wire feeding rate of 2 m/min.

2.2 Weld inspection with X-rays

Non-destructive testing with X-rays was carried out on the welded specimens to detect the defects in the weld and to quantify the shape and location of the defects if there were any. Figure 1 shows images of tensile specimens taken from the two-dimensional X-ray radiographs within a view box. It can be seen that there are no welding defects in the tensile specimen 1, as shown in Fig. 1a, and there is one porosity each observed in the welds of the tensile specimens 2 and 3 (the black points in Fig. 1b, c). The sizes of the porosities can be measured by magnifying the ruler scale. In order to simplify the complex geometric problem of the porosity shapes in

Table 1 Chemical composition of Al-Li alloy 2A97 and the filler wire ER 2319 (in wt%)

	Cu	Li	Mg	Si	Fe	V	Zr	Zn	Mn	Ti	Al
2A97	3.5–4.1	1.3–1.6	0.2–0.6	–	–	–	0.08–0.16	0.4–0.8	0.2–0.6	–	Bal.
ER2319	5.8–6.8		0.2–0.4	0.2	0.3	0.05–0.15	0.1–0.2	0.1	0.2–0.4	0.1–0.2	Bal.

the tensile specimens, the shape of all the porosities was assumed to be spherical and the diameters of spheres can be determined by measuring the diameters of black points in the radiographs. The dimensions of porosities in the tensile specimens 2 and 3 are provided in Table 2.

2.3 Uniaxial tensile test

Dog bone-shaped tensile samples were cut out of the welded blanks, with the weld seam being perpendicular to the loading condition, as illustrated in Fig. 2. The dimensions of the tensile specimens are given in Fig. 2. Uniaxial tensile tests were carried out following the international standard ISO 6892 (2009). In all the tensile tests, a constant crosshead speed of 0.03 mm/s was employed. Three tensile specimens, namely specimen 1 free of defects in the weld and specimens 2 and 3 with a pore of different sizes in the weld, were studied so as to investigate the effects of porosities on the global tensile behaviour of welded specimens.

2.4 Strain mapping by the digital imagine correlation system

The strain distributions within the specimen during tension were captured using digital image correlation (DIC), as this technique allows the local displacements and strains of the entire specimen to be recorded. Another benefit of this method is that the measurements were taken optically without the need to attach strain gauges to the specimen. With the capability to capture large strains, the DIC technique can be performed with high resolution and accuracy over a wide dynamic range. The specimen was prepared by firstly spraying the entire specimen with black paint to produce a black layer followed by spraying on white speckles stochastically on top of the material surface, as shown in Fig. 3a, b. During testing, the deformation of the welded specimen was measured by observation with a special camera. This procedure allows the determination in a plane parallel to the image plane of the camera. The recorded images were then imported into ARAMIS [32], in which a region of the specimen was selected. ARAMIS recognises the surface structure of the measuring object in the images and allocates coordinates to the image pixels. The first image in the captures represents the undeformed state of the object as well as the reference image.

The thickness and hardness profiles before the uniaxial loading were used to determine the three different zones (weld zone, HAZ and base metal). The local zones were therefore identified within the gauge length of 80 mm, as shown in Fig. 3b. The ARAMIS calculated the displacements and deformation of each zone by analysing the shift and/or distortion in
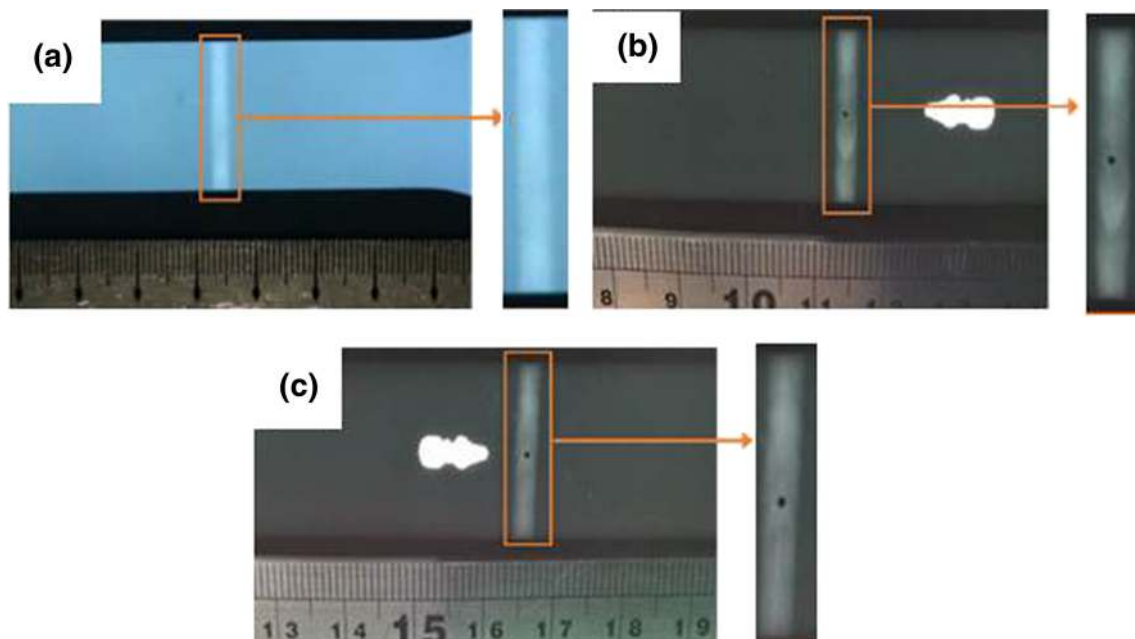
Fig. 1 X-ray radiographs for **a** specimens 1, **b** specimen 2 with a porosity diameter of 0.35 mm and (**c**) specimen 3 with a porosity diameter of 0.5 mm

Table 2 Dimensions for porosities in the tensile specimens

Specimen no.	Quantity of porosity	Diameter of porosity (mm)
1	0	0
2	1	0.35
3	1	0.5

little facet elements determined in the reference image [32]. The local strains were subsequently obtained, as shown in Fig. 3c, where the red point (with high strains) in the centre of the weld zone is a pore. The dimensions (shape and size) for each zone have been measured prior to testing, and the results are detailed in Sect. 3.2. Due to the thickness variations in the local zones, the local stress was calculated by dividing the force by the corresponding initial cross-sectional area. With reference to the time, the measured local strain and the calculated local stress were combined into the local stress–strain curves of the individual zones, as plotted in Fig. 4.

3 Tensile behaviour and development of a post-weld strength prediction model

3.1 Tensile properties of welded specimens

The stress–strain curves of 2A97-T3 Al-Li alloy before welding (parent material) and after welding (without any visible defects in the weld) are plotted in Fig. 4. It is clearly shown that both tensile strength and ductility decreased remarkably after LBW. The ultimate tensile stress (UTS) has a reduction by 30% after welding, and the ductility was reduced from 14.3% to approximately 2%.

As shown in Fig. 4, the base metal, HAZ and weld zone exhibited distinctly different local mechanical behaviour. The materials in the weld zone exhibited the lowest strength, the HAZ had a medium strength and the base metal maintained the highest strength. Due to the low heat input and high cooling rate resulting from a high welding speed, the laser-welded joint is characterised by a fine-grained weld seam and a narrow HAZ. The advantages make the joint mechanical properties superior to those in other fusion welding processes

with a lower power density [33]. The HAZ is softened by the heat input from the laser beam and the subsequent cooling after welding process. The degraded mechanical properties of the weld zone are strongly influenced by many factors [34], e.g. microstructure, defect, chemical composition, the distribution of precipitates, stress concentration induced by weld reinforcement, etc.

An interesting observation in Fig. 4 is that the ductility or elongation of the overall welded specimen is significantly lower than that of all the zones present in the material. The reason for this is that most of the deformation occur at the HAZ and weld zones that make up a smaller proportion of the specimen. Table 3 shows the engineering strains and the increases in length of the individual zones for the specimen tested in Fig. 4. It is important to point out that the stress strain curve for the parent material plotted in Fig. 4 was obtained from a separate test with only the parent material, as this data is used for the calibration of the model. Therefore, the strain at failure for the base material zone in Table 3, which is the strain when the welded specimen failed, is lower than that in Fig. 4 because the welded specimen fails when either the HAZ or weld zone fractures.

As seen in Table 3, due to the significantly lower proportions of the initial length of the HAZ and weld zones, the total increase in length of these zones is low, even though the engineering strains of these zones are high. For example, the weld zone that has 7.064% of the strain only leads to a small increase in the overall specimen length of 0.445 mm. On the other hand, the base metal zone contributes to a larger increase in overall specimen length of 0.907 mm. This increase in length is almost 60% of the increase in overall length according to Table 3, even though its elongation is only 0.639%, which is significantly lower than the other zones. Comparing the elongation of the base material in Table 3 of 0.639% with the elongation of the parent material in Fig. 4 of 14.26% suggests that the parent material still requires significantly more deformation when the welded specimen fractures at either the HAZ or the weld zone. The elongation of the 0.639% of the parent material that contributes to the largest proportion of the increase in length is lower than the overall elongation of 0.950% of the entire welded specimen. Therefore, the lower elongation of the welded specimen can be attributed to the
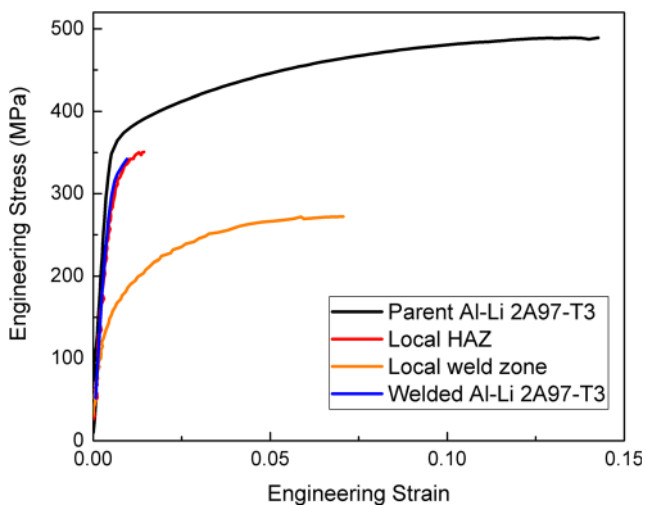
Fig. 2 Tensile specimen configurations (unit: mm)
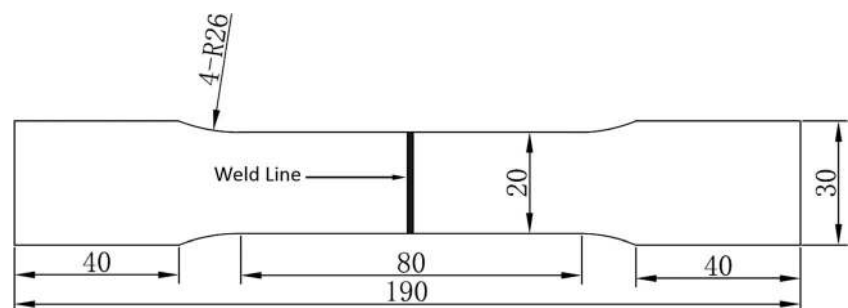
Fig. 3 **a** DIC tensile specimen, **b** weld zone and heat-affected zone and **c** strain field of the specimen under uniaxial load
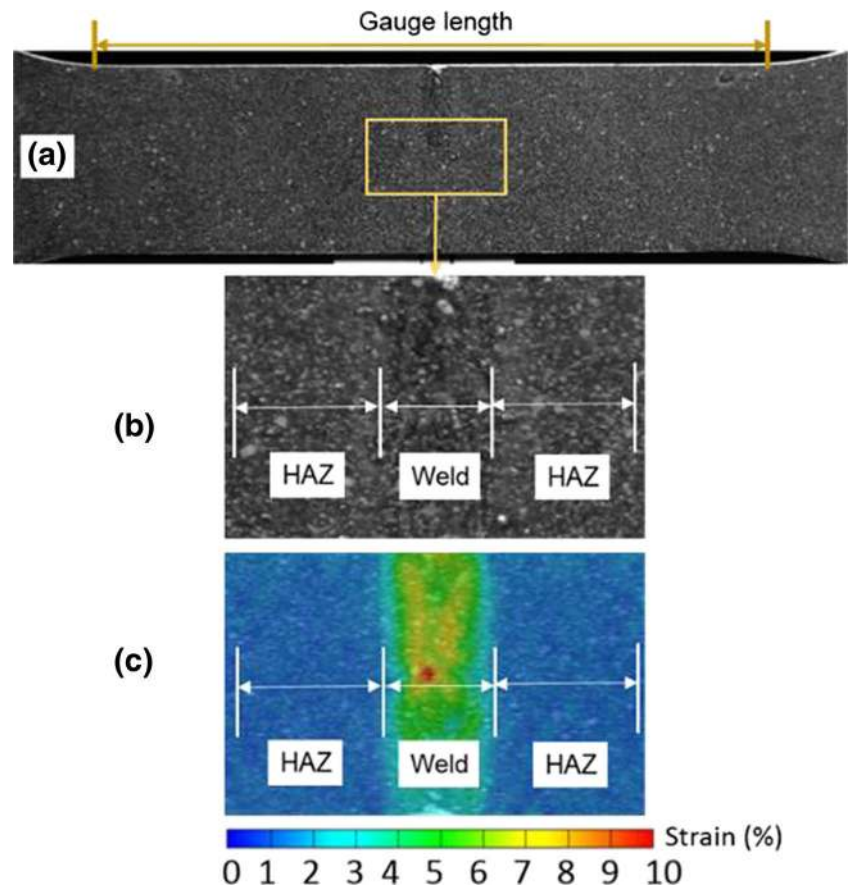
lower proportion of the HAZ and weld zones compared to the base material leading to lower increases in overall length. The HAZ and weld zones that fractures significantly earlier compared to the base material, while the stronger base material does not undergo much deformation, leading to an overall lower elongation of the welded specimen. This effect is also present in the specimens with porosity. The variations in the local strains for each zones will be discussed in further detail in Sect. 4.

The presence of porosity can reduce the load area of the weld and cause stress concentration. Figure 5 shows the comparison of 0.2% offset yield stress among the specimens with different porosity sizes. The yield stress of specimen 1 without porosity was found to be higher than that of specimens 2 and 3 with a single porosity. The yield strength of specimen 2 with a porosity diameter of 0.35 mm is higher than that of specimen 3 with a porosity diameter of 0.5 mm, because the diameter of the porosity inside specimen 2 is larger than that inside specimen 3. Generally, the yield stress decreased with the increasing pore diameter in the weld. The porosity also changed the fracture behaviour of the welded specimens as evidenced in Fig. 6. During deformation, the tensile specimen 1 (defect free) broke due to large straining in the weld zone, while failure initiated in the porosities of specimens 2 and 3 and then fractured throughout the remaining weld zone.

**3.2 Determination of zones in welded specimens to be used in the models**

As seen in the previous section, the mechanical property of the material at the vicinity of the weld zone is different from the parent material. To account for the difference in the mechanical

Fig. 4 Typical tensile curves for laser-welded specimens without defect in the weld

Table 3   Stress, strains and elongation at failure of the specimen in Fig. 4

Zone	Engineering strain at failure ($\times 10^{-3}$)	Initial length of zone, L_0 (mm)	Increase in length at failure, ΔL (mm)	Proportion of length increment of zone (%)
Base	6.39	142.0	0.907	59.68
HAZ	14.34	11.7	0.168	11.04
Weld	70.64	6.3	0.445	29.28
Overall	9.50	160.0	1.520	100.00

properties of the specimen, the specimen is separated into three zones, which are the weld zone, the heat-affected zone and the base metal, each of them are assumed to have different mechanical properties in the model described later.

The hardness across the specimen is measured to determine the region for each individual zone. The hardness test was performed using a Vickers micro-hardness tester with a load of 20 g and a dwell time of 12 s. The hardness profile is plotted in Fig. 7, where the three zones (base metal, HAZ and weld zone) can be identified by a sharp change in the measured hardness. As seen in Fig. 7, there is a region in the specimen with a hardness that is identical to an unwelded specimen of more than 120 HV. This region is denoted as the base metal zone and assumed to have the same material properties as the parent material. Adjacent to the base material is a region with a slightly lower hardness, as seen in Fig. 7. This region is the heat-affected zone, which is a part of the specimen that was not melted during the welding process but undergoes changes in material properties due to temperature increases from heat conduction from the weld zone. The final region with the lowest hardness is the weld zone, which is the region that has melted during the welding process. Due to excess material being added during the welding process, the thickness of the weld zone is slightly larger than the HAZ and base material as seen in Fig. 7a. In order to account for the porosity in the weld,
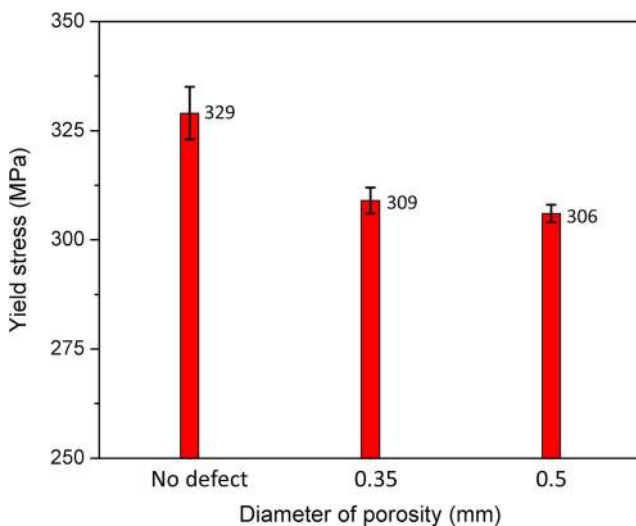
an additional zone, denoted as the defect zone in this study, is added to the model. The defect zone is assumed have the same material as the weld zone, with the only exception having a reduced thickness compared to the other weld zone. The dimensions of the defect zone were determined from the size of the pore.

The partitioning of the specimen into the four zones in this study is shown in Fig. 8, where the subscripts A, B, C and D are used to denote the base metal, weld zone, HAZ and defect zones, respectively. In order to simplify the analysis, the thickness of the weld zone is assumed to be uniform, while the base metal and HAZ were assumed to have the same thickness, in the model.

A total of three specimens, one defect free, one with a 0.35-mm pore and one with a 0.5-mm pore, were studied in this work. The lengths of the individual zones were determined from the hardness measurements described previously. Since the three specimens were machined from a single laser-welded blank, with the only difference being the size of the porosity, the length of the HAZ and base metal is identical for all three specimens. Additionally, the width of the specimens was also machined to be uniform across the entire specimen.

The thicknesses of the base, HAZ and weld zones were measured using a Vernier calliper. However, the defect zone is modelled to be a zone with the properties of the weld zone of length L_D, but with a reduction in the thickness, R in Fig. 8, which is dependent on the size of the porosity. In order to determine the value of R in Fig. 8, the porosity was assumed to be spherical and the diameter was measured from the radiograph in Fig. 1. This allows the volume of the pore, V, to be determined by Eq. (1). In the model, the initial length of defect zone, L_{D0}, is assumed to be equal to the diameter of the pore from the radiograph, as shown in Eq. (2). Moreover, the volume removed from the base material in defect zone is also equal to that of the pore, as seen in in Eq. (3).

$$V = \frac{4}{3}\pi\left(\frac{D}{2}\right)^3 \tag{1}$$

$$L_{D0} = D \tag{2}$$

$$V = L_{D0}WR \tag{3}$$

where V is the volume of the pore and also the volume removed from the base material in defect zone, D is the diameter

Fig. 5   Trend of yield strength of welded specimens with a range of porosity diameters

Fig. 6 The tensile tested specimens. **a** Fracture for specimen 1 without defect. **b** Fracture for specimen 2 with a porosity diameter of 0.35 mm. **c** Fracture for specimen 3 with a porosity diameter of 0.5 mm
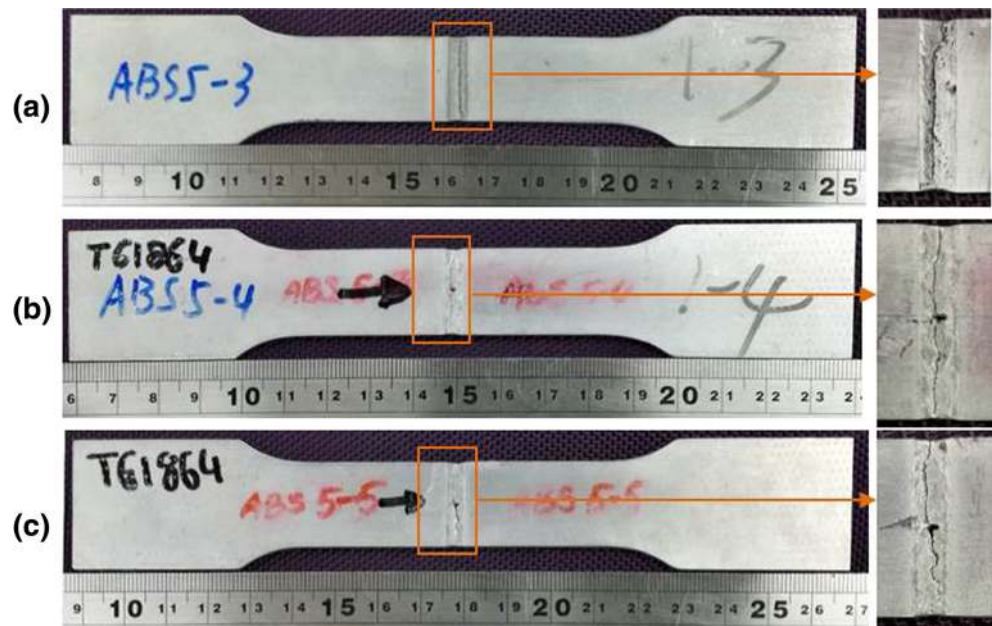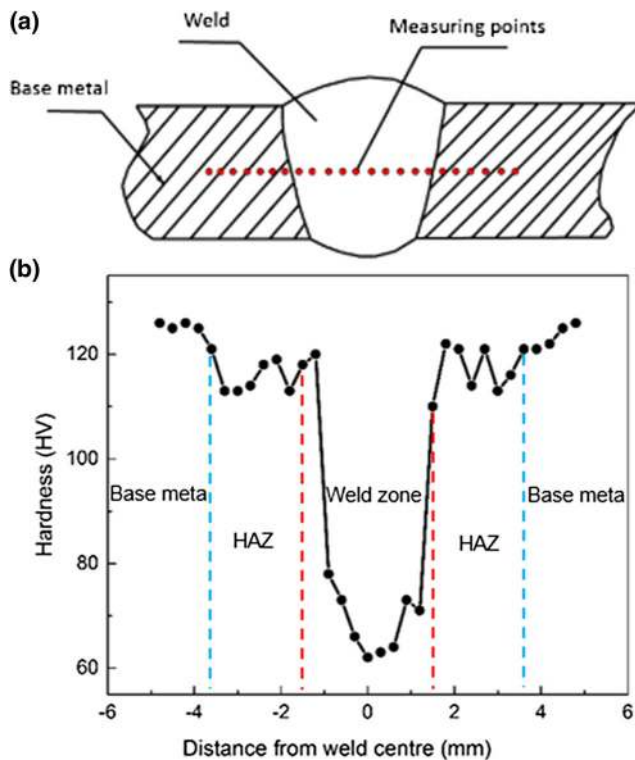

of the pore, W is the weld width, R is the reduction in equivalent thickness of the defect zone which was mathematically converted from a spherical pore into a cuboid defect and L_{D0} is the initial length of the defect zone.

Therefore, the equivalent thickness reductions (R) in the defect zone, which were calculated by substituting the equations above, are listed in Table 4. The partitioning of the

Fig. 7 **a** Sketch map of measuring points for micro-hardness. **b** Profiles of the micro-hardness for the welded joint

specimen into these zones and their measured dimensions in Table 4 were then used in the modelling study that will be described in the next section.

3.3 Post-weld strength prediction model

After LBW, the Al-Li blanks would have a weld metal zone and a heat-affected zone that have an overall lower strength compared to the parent material. This will reduce significantly the global material response of the specimens. A post-weld strength prediction (PWSP) model has been developed to characterise the degradation in the global strength [35]. Although more robust models are available in the literature, the PWSP was selected for this study as it is sufficiently accurate while offering other benefits. Firstly, the material parameters required for each zone in the model, as seen in Fig. 8, can be determined from a tensile specimen, significantly reducing the amount of experiments to calibrate the model. Additionally, the simplicity of the PWSP model facilitates its use as it is simple to setup, has minimal computational costs and can explain the deformation behaviour in an easily comprehensible manner. These benefits make the PWSP model a suitable choice for this study. However, welding defects are detrimental to the post-weld strength. Therefore, the PWSP model was extended to include a defect zone to investigate the effects of porosities on the global mechanical properties of the laser-welded Al-Li specimens.

3.3.1 Constitutive equations

The model was developed based on plastic deformation of metals under plane stress conditions. In this study, direction 1 is the axial direction of the specimen, direction 2 is the

Fig. 8 Schematic of four zones for the PWSP model: L_A length of the base metal, L_C length of the HAZ, T_A thickness of base metal (or HAZ), $L_{B\text{-top}}$ weld length at the top side, $L_{B\text{-bottom}}$ weld length at the bottom side, L_B average weld length, L_D length of defect zone, R equivalent height of porosity or reduction in equivalent thickness of the defect zone, W weld width (or specimen width), T_B weld thickness
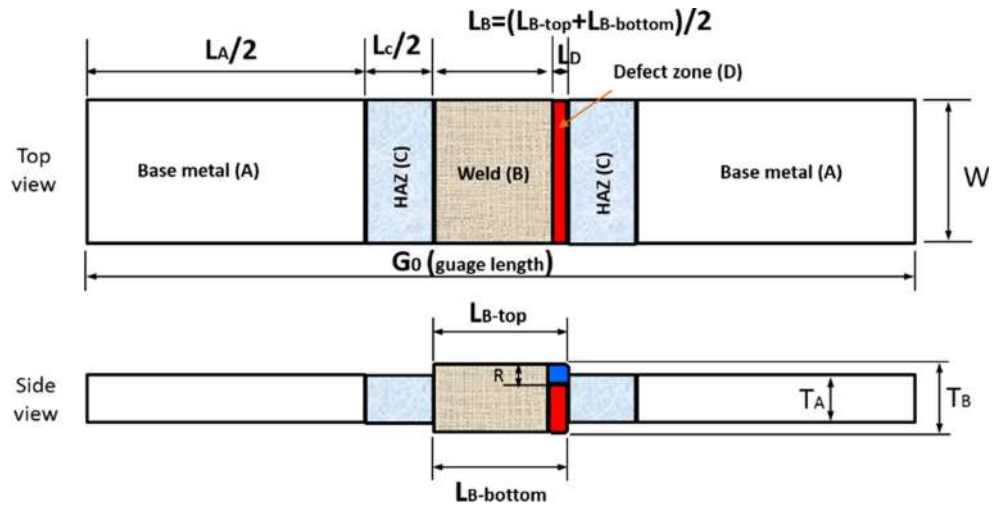
direction across the width of the specimen and direction 3 is normal to the plane.

The four zones were modelled separately as the homogenous material being loaded under plane stress conditions ($\sigma_3 = 0$). The entire specimen in Fig. 8 is modelled using four zones designated as sections A, B, C and D for the base metal, the HAZ, the weld zone and the defect zone, respectively. The end of the weld zone is treated as a symmetrical boundary condition. The plastic deformation behaviour of the laser-welded joints was described by a power law relationship as follows.

$$\overline{\sigma} = \begin{cases} E\overline{\varepsilon}, & \overline{\varepsilon} \leq \varepsilon_p \\ k\overline{\varepsilon}^n, & \overline{\varepsilon} > \varepsilon_p \end{cases} \quad (4)$$

where $\overline{\sigma}$ is the von Mises stress which can be calculated by Eq. (5), E is the Young's modulus, ε_p is the strain when yielding initiates, k and n are material parameters determined using experimental results and $\overline{\varepsilon}$ is the equivalent strain described by Eq. (6).

$$\overline{\sigma} = \sqrt{\frac{1}{2}\left[(\sigma_1 - \sigma_2)^2 + \sigma_1^2 + \sigma_2^2\right]} \quad (5)$$

$$d\overline{\varepsilon} = \sqrt{\frac{2}{3}\left(d\varepsilon_1^2 + d\varepsilon_2^2 + d\varepsilon_3^2\right)} \quad (6)$$

The volume of metallic alloys, in general, is constant, suggesting that the change in strain increments follows the following equation.

$$d\varepsilon_1 + d\varepsilon_2 + d\varepsilon_3 = 0 \quad (7)$$

In this study, the material is modelled using the Levy–Mises flow rule during plastic deformation as described by the following equation [36].

$$\frac{d\varepsilon_1}{\sigma_1 - \frac{1}{3}(\sigma_1 + \sigma_2 + \sigma_3)} = \frac{d\varepsilon_2}{\sigma_2 - \frac{1}{3}(\sigma_1 + \sigma_2 + \sigma_3)}$$
$$= \frac{d\varepsilon_3}{\sigma_3 - \frac{1}{3}(\sigma_1 + \sigma_2 + \sigma_3)} \quad (8)$$

β is the strain increment ratio, describes as follows.

$$\beta = \frac{d\varepsilon_2}{d\varepsilon_1} \quad (9)$$

The Young's modulus, E, was set to 73 GPa for the Al-Li alloy. True stress and strains were used in Eqs. (4)–(9).

3.3.2 Boundary conditions

The base metal (zone A) is deformed under uniaxial loading condition, as no stresses were applied in the directions parallel to the width and thickness of the specimen. This suggests that the strain increment ratio of zone A, β_A, is − 0.5. The axial strain in zone A, ε_{1A}, is an independent variable. The strains in the other directions were found by solving Eqs. (4)–(9). The materials in the other zones were then calculated by using the constitutive equations of the material and enforcing force

Table 4 Dimensions for each local zone of the welded specimens based on Fig. 8 (unit: mm)

	L_{A0}	L_{B0}	L_{C0}	L_{D0} (D)	R	T_{A0} (T_{C0})	T_{B0}	W_0
1 (defect free)	71.00	5.85	3.15	–	–	1.43	1.81	20
2 (0.35 mm pore)	70.65	5.82	3.18	0.35	0.0032	1.43	1.80	20
3 (0.5 mm pore)	70.50	5.83	3.17	0.50	0.0065	1.43	1.82	20
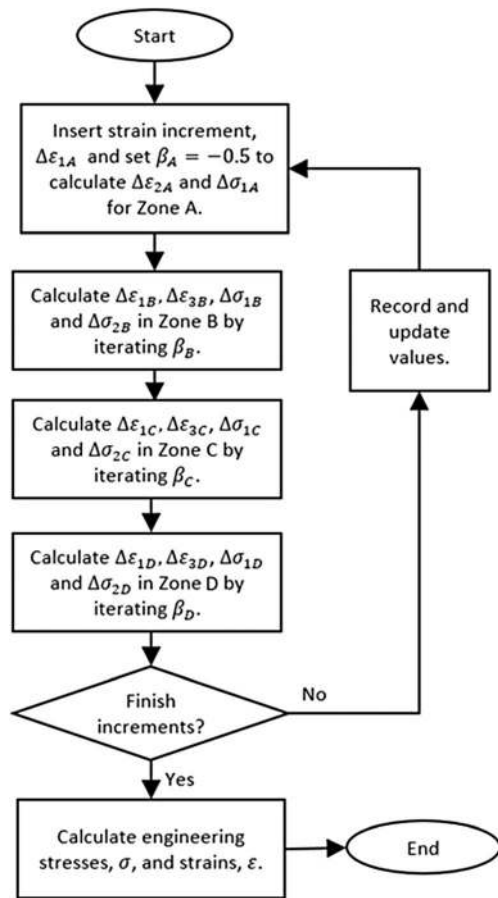
Fig. 9 Flow chart showing the numerical calculation procedure

Fig. 10 Tensile curves for different zones: local HAZ, local weld and base metal

balance and continuity at the boundary of the two zones, which can be described by the following equations.

$$\sigma_{1B} = \frac{W_A T_A}{W_B T_B} \sigma_{1A} \tag{10}$$

$$d\varepsilon_{2B} = d\varepsilon_{2A} \tag{11}$$

$$\sigma_{1C} = \frac{W_B T_B}{W_C T_C} \sigma_{1B} \tag{12}$$

$$d\varepsilon_{2C} = d\varepsilon_{2B} \tag{13}$$

$$\sigma_{1D} = \frac{W_C T_C}{W_D T_D} \sigma_{1C} \tag{14}$$

$$d\varepsilon_{2D} = d\varepsilon_{2C} \tag{15}$$

where W and T are the width and thickness of the individual zones, respectively.

Table 5 Material constants for the local zones used in the PWSP model

Power law coefficients	Base zone	HAZ	Weld zone	Defect zone
E (GPa)	73	73	73	73
K (MPa)	635	710	610	610
n	0.12	0.16	0.26	0.26

The strains in HAZ (zone B), weld zone free of defects (zone C) and weld zone with defects (zone D) were assumed to be uniform.

3.3.3 Numerical calculations

Equations (4)–(15) were solved numerically using the central difference method. The steps taken in this paper were similar to those in a previous study [35] but with the addition of an extra defect zone (namely zone D). In each step, the strains and stresses $\Delta\varepsilon_{2A}$, $\Delta\varepsilon_{3A}$ and $\Delta\sigma_{1A}$ in zone A were first calculated by solving the constitutive equations for the material for a given $\Delta\varepsilon_{1A}$, with β_A being set to -0.5. After that, the values of $\Delta\varepsilon_{1B}$, $\Delta\varepsilon_{3B}$, $\Delta\sigma_{1B}$ and $\Delta\sigma_{2B}$ for the next zone, zone B, were calculated by solving the constitutive equations and applying the boundary conditions stated previously. A numerical iteration procedure using an optimisation procedure was performed by iterating the value of β_B, to solve the required equations. This procedure is repeated for the subsequent zones (zones C and D). Figure 9 shows a flow chart for the calculation procedure.

Finally, the global engineering stress δ_n and engineering strain e_n were calculated by Eqs. (16)–(20) after the stress strain behaviour of the specimen was calculated.
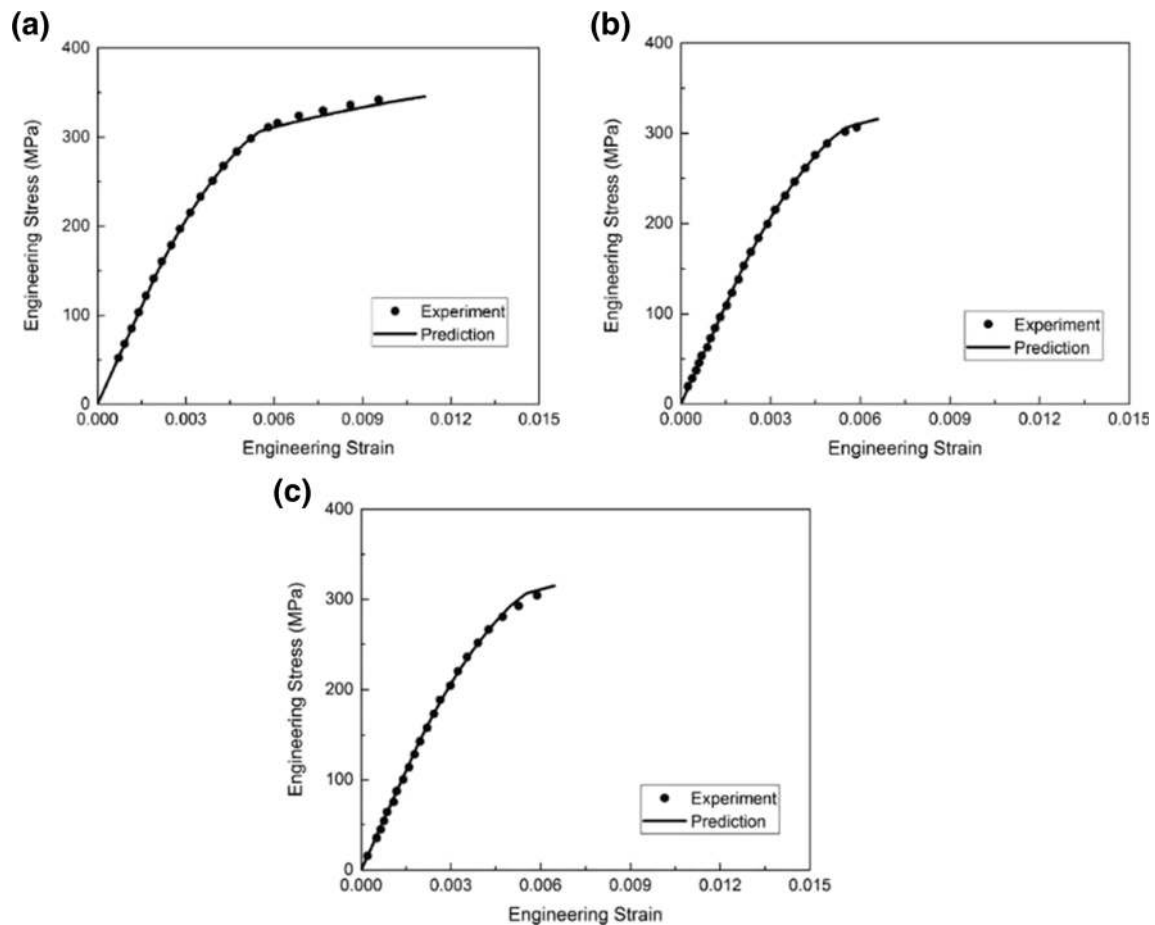
$$\delta_n = \frac{\delta_{A,n} W_{A,n} T_{A,n}}{W_{A,0} T_{A,0}} \tag{16}$$

$$e_n = \frac{(L_{A,n} + L_{B,n} + L_{C,n}) - (L_{A,0} + L_{B,0} + L_{C,0})}{L_{A,0} + L_{B,0} + L_{C,0}} \tag{17}$$

$$W_n = W_{n-1} + \Delta\varepsilon_{2,n}(W_{n-1}) \tag{18}$$

$$T_n = T_{n-1} + \Delta\varepsilon_{3,n}(T_{n-1}) \tag{19}$$

$$L_n = L_{n-1} + \Delta\varepsilon_{1,n}(L_{n-1}) \tag{20}$$

Fig. 11 Comparison of stress–strain curves between prediction (lines) and experiment (symbols). **a** Specimen 1 without defect. **b** Specimen 2 with a porosity diameter of 0.35 mm. **c** Specimen 3 with a porosity diameter of 0.5 mm

where n denotes the increment number and W, T and L are the real-time width, thickness and length, respectively. All the dimensions are updated during calculation at every increment according to Eqs. (18)–(20).

3.4 Calibration of local stress–strain curves

The plastic stress–strain behaviour of each zones in the material is described using a power law relationship, where the material constants need to be calibrated. Table 5 shows all the material constants for each zones used in the model. The local stress–strain curves of the HAZ and weld zone were obtained by DIC, as plotted in Fig. 4. The calibration results are shown in Fig. 10, where the predicted results are shown in solid lines and the experimental data are shown in symbols. As seen in the figure, the calibrated results fit the experimental results very well. This validates the values of k and n in this study. Therefore, the parameters for each zone in Fig. 10 were validated. The engineering stress and strain values were then converted to true stress and strains for the PWSP model.
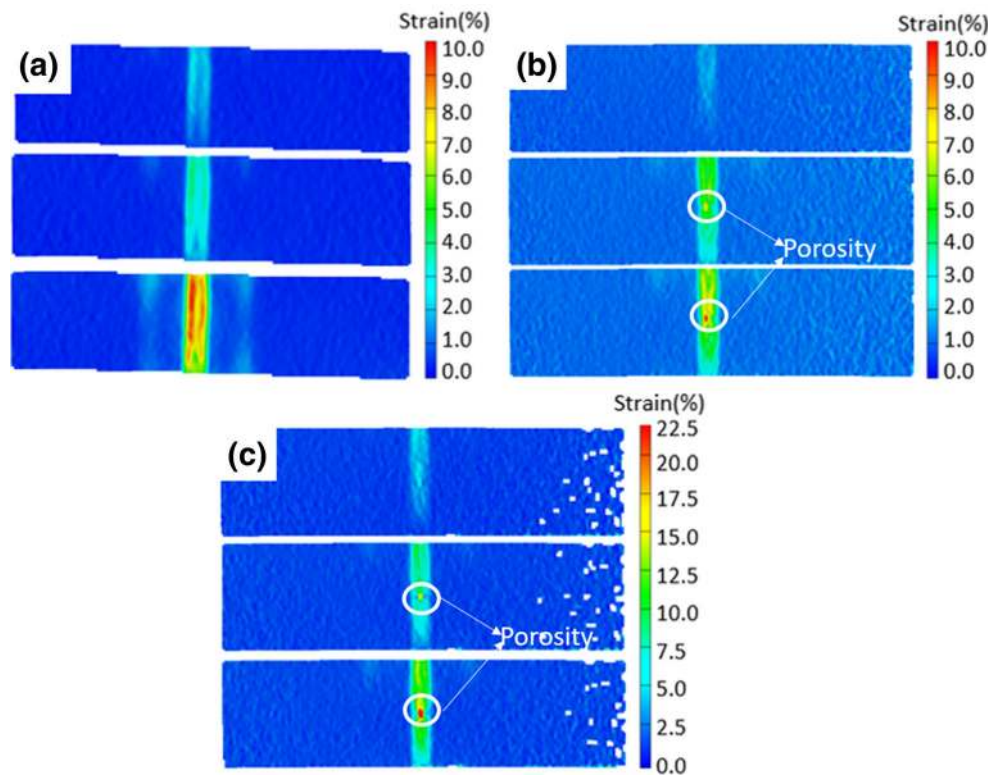
3.5 Prediction of the global stress

The geometries (Table 4) and calibrated material constants (Table 5) have been used in calculation to predict the overall strength. The predicted results (in solid lines) and experimental curves (in symbols) are presented in Fig. 11, from which very good agreement is achieved. The comparison of 0.2% offset yield stress values between the model and the experiments is listed in Table 6. For the defect-free case, the model shows a yield stress of 314 MPa, deviating from the tested proof strength (329 MPa) by 4.5%. The deviation decreased to 1 and 1.6% in predicting the yield stress of specimens with

Table 6 Comparison of predicting yield stress and experimental yield stress

Sample no.	Global 0.2% yield stress (MPa)	Modelling (MPa)	Deviation (%)
1	329	314	4.5
2	309	312	1
3	306	311	1.6

Fig. 12 Strain evolution for tensile specimens. **a** Specimen 1 without defect. **b** Specimen 2 with a porosity diameter of 0.35 mm. **c** Specimen 3 with a porosity diameter of 0.5 mm
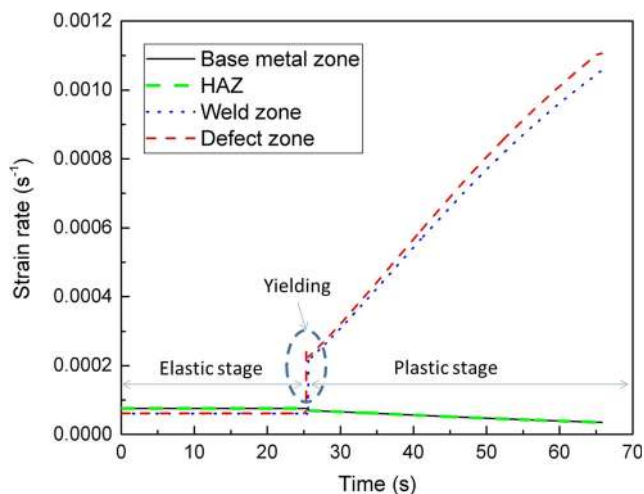

porosities, respectively. The results demonstrate that the model, with the consideration of defects in the 2A97 Al-Li alloy laser-welded specimens, can successfully predict evolution of the global flow stress and the 0.2% yield stress.

4 Discussion

The strain distributions in specimen 1, specimen 2 and specimen 3 are shown in Fig. 12a–c, respectively. For the

Fig. 13 Strain rate–time curves for tensile specimen 2 with a porosity diameter of 0.35 mm

specimen 1 (defect free), the peak strains are distributed intensively in the weld zone (Fig. 12a). At the early stage of the tensile test, the deformation started and concentrated in the weld zone; with the increasing of strain, a part of the materials in HAZ participated in the deformation too due to the work hardening of the weld zone, but the peak strains still located in the weld zone; the base metal almost had no deformation during the whole process due to its higher strength, which is consistent with the hardness test result. Similar deformation behaviour of strain concentration in the weld zone was also observed in the specimen 2 and specimen 3 with a defect in the weld. However, the different part of the strain distributions for specimen 2 and specimen 3 is that the peak values of strain are localised around the porosity in the weld zone (Fig. 12b, c). It is also obvious that the strains are distributed more evenly in the weld zone of specimen 1, suggesting that a larger proportion of specimen 1 undergoes plastic deformation than that in the other two specimens, which indicates that the porosities in the weld would aggravate the local deformation and impair the specimen properties.

To further investigate the effects of porosity on the deformation behaviour of laser-welded joints of 2A97-T3 Al-Li alloy, the strain rates of different zones of tensile specimen 2 with a porosity diameter of 0.35 mm were obtained for different zones. The result is shown in Fig. 13, from which one can see that the four zones could be divided into two groups: one group including the base metal zone and HAZ and the other group including the weld zone and defect zone. Both base

metal zone and HAZ had very low strain rates, and the value of strain rates for them is below 7.55×10^{-5}/s during the whole deformation process and the two distribution lines almost coincided. This is because both zones had higher strength than the weld zone. Therefore, both of them resisted deformation during the tensile process, which is in good agreement with the experimental results shown in Fig. 12. However, for the other group including the weld zone and defect zone, two obviously different stages (elastic stage and plastic stage) were observed. During the elastic stage, the strain rate was constant due to the constant Young's modulus. At 25.60 s, the material yielded, and the strain rate increased to a higher level immediately as seen in Fig. 13. After that, both strain rates of the weld zone and defect zone increased almost linearly with time. At the early stage of plastic deformation, the two had similar strain rate values, but with the increase of strain, the defect zone had higher strain rate than the weld zone and the gap between them gradually increased with time. When stress around the porosity reached its limit, a crack nucleated and propagated quickly leading to the specimen failure. Therefore, the porosity in the weld significantly reduced the ductility of the specimen.

5 Conclusions

The effects of porosity on the mechanical properties of fibre laser-welded 2A97-T3 Al-Li alloy joint were studied both experimentally and numerically in this paper. Uniaxial tensile test together with the adoption of DIC technique has been used to characterise the local mechanical properties of the base material, heat-affected zone and weld zone in the welded specimens. Both the yield strength and the ductility of the tensile specimen decreased with the existence of porosity in the weld zone. The post-weld strength prediction model was extended to include the effects of the porosity and was further developed to predict the global properties of the butt joints, by employing a defect zone. The model has been validated through experiments, where it predicted the global flow stress curves as well as the 0.2% proof strength of welded 2A97-T3 Al-Li alloy accurately with a deviation less than 5%. The major factors affecting the global strength of the welded specimens were found to be the local properties and dimensions of the defect zone and the weld zone. After welding, the strength of the weld zone was lower than that of the HAZ and base metal. The strains were concentrated in the weld zone during deformation, which subsequently impaired the deformation uniformity. When there exist porosities in the weld zone, the local deformation in the weld zone was concentrated around the porosities. Higher strain rate was found in the defect zone than the weld zone, which is deemed to accelerate the failure of the specimen and reduce the global ductility remarkably.

References

1. Sundaresan S, Janaki Ram GD, Murugesan R, Viswanathan N (2000) Combined effect of inoculation and magnetic arc oscillation on microstructure and tensile behaviour of type 2090 Al–Li alloy weld fusion zones. Sci Technol Weld Joi 5:257–264
2. Kostrivas A, Lippold JC (1999) Weldability of Li-bearing aluminium alloys. Int Mater Rev 44:217–237
3. Hector LG, Chen Y-L, Agarwal S, Briant CL (2004) Texture characterization of autogenous Nd:YAG laser welds in AA5182-O and AA6111-T4 aluminum alloys. Metall Mater Trans A 35:3032–3038
4. Peng Y, Fu Z, Wang W, Zhang J, Wang Y, Wang H, Zhang Q (2008) Phase transformation at the interface during joining of an Al–Mg–Li alloy by pulsed current heating. Scripta Mater 58:49–52
5. Padmanabham G, Pandey S, Schaper M (2005) Pulsed gas metal arc welding of Al–Cu–Li alloy. Sci Technol Weld Joi 10:67–75
6. Solórzano IG, Darwish FA, de Macedo MC, de Menezes SO (2003) Effect of weld metal microstructure on the monotonic and cyclic mechanical behavior of tig welded 2091 Al–Li alloy joints. Mater Sci Eng A 348:251–261
7. Li S, Chen G, Zhou C (2015) Effects of welding parameters on weld geometry during high-power laser welding of thick plate. Int J Adv Manuf Tech 79:177–182
8. Luo Y, Tang X, Lu F (2014) Experimental study on deep penetrated laser welding under local subatmospheric pressure. Int J Adv Manuf Tech 73:699–706
9. Hamidinejad SM, Hasanniya MH, Salari N, Valizadeh E (2013) CO_2 laser welding of interstitial free galvanized steel sheets used in tailor welded blanks. Int J Adv Manuf Tech 64:195–206
10. Ion JC (2000) Laser beam welding of wrought aluminium alloys. Sci Technol Weld Joi 5:265–276
11. Zhao H, White DR, DebRoy T (1999) Current issues and problems in laser welding of automotive aluminium alloys. Int Mater Rev 44:238–266
12. Williams JC, Starke EA Jr (2003) Progress in structural materials for aerospace systems[1]. Acta Mater 51:5775–5799
13. Chen H-C, Pinkerton AJ, Li L (2011) Fibre laser welding of dissimilar alloys of Ti-6Al-4V and Inconel 718 for aerospace applications. Int J Adv Manuf Tech 52:977–987
14. Brenner B, Standfuß J, Dittrich D, Winderlich B, Liebscher J, Hackius J (2008) Laser beam welding of aircraft fuselage structures, International Congress on Applications of Lasers & Electro Optics (ICALEO). Temecula, USA
15. Mueller-Hummel P, Ferstl S, Sengotta M, Lang R (2003) Laser beam welding of high stressed, complex aircraft structural parts. First International Symposium on High-Power Laser Macroprocessing, Osaka
16. Xu F, Chen L, Li SG, LI XY, Yang J (2011) Microstructure and mechanical properties of Al-Li alloy by laser welding with filler wire. Rare Metal Mat Eng 40:1775–1779

17. Cui L, Li X, He D, Chen L, Gong S (2012) Effect of Nd:YAG laser welding on microstructure and hardness of an Al–Li based alloy. Mater Charact 71:95–102

18. Matsunawa A (2001) Problems and solutions in deep penetration laser welding. Sci Technol Weld Joi 6:351–354

19. Zhang X, Yang W, Xiao R (2015) Microstructure and mechanical properties of laser beam welded Al–Li alloy 2060 with Al–Mg filler wire. Mater Design 88:446–450

20. Fu B, Qin G, Meng X, Ji Y, Zou Y, Lei Z (2014) Microstructure and mechanical properties of newly developed aluminum–lithium alloy 2A97 welded by fiber laser. Mater Sci Eng A 617:1–11

21. Wu SC, Yu C, Zhang WH, Fu YN, Helfen L (2015) Porosity induced fatigue damage of laser welded 7075-T6 joints investigated via synchrotron X-ray microtomography. Sci Technol Weld Joi 20:11–19

22. Çam G, İpekoğlu G (2017) Recent developments in joining of aluminum alloys. Int J Adv Manuf Tech 91:1851–1866

23. Xiao R, Wuxiong Y, Kai C (2007) Porosity characterization in laser welds of Al-Li alloy 1420. Appl Laser 27:13–17

24. Kai C, Wuxiong Y, Rongshi X (2010) Direct laser welding for Al-Li alloy plate without the cleaning of surface film. Springer, London

25. Whitaker IR, McCartney DG, Calder N, Steen WM (1993) Microstructural characterization of CO$_2$ laser welds in the Al-Li based alloy 8090. J Mater Sci 28:5469–5478

26. Matsunawa A, Mizutani M, Katayama S, Seto N (2003) Porosity formation mechanism and its prevention in laser welding. Weld Int 17:431–437

27. Matsunawa A, Kim J-D, Seto N, Mizutani M, Katayama S (1998) Dynamics of keyhole and molten pool in laser welding. J Laser Appl 10:247–254

28. Seto N, Katayama S, Mizutani M, Matsunawa A (2000) Relationship between plasma and keyhole behavior during CO$_2$ laser welding. High-Power Lasers in Manufacturing, Osaka

29. Abdullah K, Wild PM, Jeswiet JJ, Ghasempoor A (2001) Tensile testing for weld deformation properties in similar gage tailor welded blanks using the rule of mixtures. J Mater Process Tech 112:91–97

30. Liu S, Chao YJ (2005) Determination of global mechanical response of friction stir welded plates using local constitutive properties. Model Simul Mater Sci Eng 13:1–15

31. Lockwood WD, Tomaz B, Reynolds AP (2002) Mechanical response of friction stir welded AA2024: experiment and modeling. Mater Sci Eng A 323:348–353

32. GOM (2007) ARAMIS user manual. GOM mbH, Braunschweig

33. DebRoy T, David SA (1995) Physical processes in fusion welding. Rev Mod Phys 67:85–112

34. Lee MF, Huang JC, Ho NJ (1996) Microstructural and mechanical characterization of laser-beam welding of a 8090 Al-Li thin sheet. J Mater Sci 31:1455–1468

35. Liu J, Wang L, Lee J, Chen R, El-Fakir O, Chen L, Lin J, Dean TA (2015) Size-dependent mechanical properties in AA6082 tailor welded specimens. J Mater Process Tech 224:169–180

36. Hosford WF (2005) Mechanical behavior of materials. UK, Cambridge